Showcasing research from Professor Teruaki Hayakawa's laboratory, Department of Materials Science and Engineering, School of Materials and Chemical Technology, Institute of Science Tokyo.

Self-assembly of semiaromatic poly(amic acid) into flower-like microparticles *via* one-step precipitation polymerization

This study investigates the self-assembly of semiaromatic poly(amic acid) (PAA) into intricate flower-like particles *via* one-step precipitation polymerization. The particle morphology is tunable from spherical to flower-like by adjusting the mixed solvent ratio. Notably, the flower-like morphology is largely retained after carbonization, yielding carbon flowers with high catalytic activity in the two-electron oxygen reduction reaction in an acidic electrolyte.

Image reproduced by permission of Yuqian Chen from *RSC Appl. Polym.*, 2025, **3**, 613.

As featured in:

See Chen *et al.*, *RSC Appl. Polym.*, 2025, **3**, 613.

ROYAL SOCIETY OF CHEMISTRY

rsc.li/RSCApplPolym

Registered charity number: 207890

RSC Applied Polymers

ROYAL SOCIETY OF CHEMISTRY

PAPER

View Article Online
View Journal | View Issue

Cite this: *RSC Appl. Polym.*, 2025, **3**, 613

Self-assembly of semiaromatic poly(amic acid) into flower-like microparticles *via* one-step precipitation polymerization†

Yuqian Chen, [a] Ryohei Kikuchi, [b] Kan Hatakeyama-Sato, [a] Yuta Nabae *[a] and Teruaki Hayakawa *[a]

Flower-like particles (FLPs) are highly attractive materials owing to their intricate morphologies and high specific surface areas. However, a definitive method for fabricating organic FLPs with unique three-dimensional morphologies has yet to be established. In this paper, we report on a synthetic route for poly (amic acid) (PAA) FLPs using a specially designed semiaromatic PAA consisting of alternate rigid aromatic segments and flexible alkyl segments *via* one-step precipitation polymerization at room temperature. The particle morphology can be tuned from spherical to flower-like by adjusting the mixed-solvent ratio. Based on small-angle X-ray scattering, wide-angle X-ray diffraction, and polarized optical microscopy analyses, the flower-like morphology is attributed to the microcrystalline structure formed by the folded and stacked alignment of the PAA precursors. Moreover, solubility plays a crucial role in determining the crystallization rate and growth mechanism, thereby leading to variations in the flower-like morphology. Notably, the flower-like morphology is preserved after thermal imidization and carbonization. The as-synthesized carbon flowers demonstrated high catalytic activity and selectivity for the 2-electron electrochemical reduction of oxygen in an acidic electrolyte, which could be attributed to the N-content of 2.72% and the efficient mass transport granted by the open structure of the unique flower-like morphology.

Received 29th October 2024,
Accepted 21st February 2025

DOI: 10.1039/d4lp00327f

rsc.li/rscapplpolym

Introduction

Polymeric particles with three-dimensional, higher-order internal and surface morphology, such as Janus,[1,2] lamella,[3,4] onion-like,[5] and golf ball-like,[6] have garnered significant interest across a wide range of application areas. The morphology control of these intricate particles often utilizes the bottom-up method, *i.e.* the self-assembly behavior of the block copolymer precisely prepared through controlled polymerization.[2–6] However, polymers synthesized *via* step-growth polymerization, such as polyimides (PIs) and their precursor poly(amic acid)s (PAAs), hardly form microphase-separated, higher-order structures when combined with other thermodynamically immiscible blocks to form diblock or triblock copolymers. This difficulty arises from the challenges in precisely controlling the molecular weight of PIs.

Among various classes of morphologies, flower-like particles (FLPs) exhibit complex, higher-order internal and surface morphologies, offering a large surface area. These characteristics make FLPs promising materials for applications in various fields, such as gas capture,[7,8] host materials for targeted drug delivery,[9] and catalyst supports.[10] So far, there are only a few reports on the successful synthesis of flower-like morphologies in the field of organic chemistry.[11–18] For example, Liu *et al.* reported the FLPs formed from precipitation polymerization of a redox-responsive liquid crystalline monomer.[15] Zhang *et al.* also reported that cellulose stearoyl esters can precipitate into FLPs in non-solvents and the flower-like morphology relates to the polymer molecular weight, concentration of the polymer solution, and the volume ratio of the mixed solvents.[16] Chen *et al.* further demonstrated the facile synthesis of polyacrylonitrile (PAN) FLPs as precursors for carbon flowers.[18] Their subsequent investigation revealed that the flower-like morphology originated from orthorhombic PAN crystals.[19] However, no universal synthesis route or formation mechanism has been identified for this complex morphology.

While morphology control of PIs is generally challenging,[20,21] Sun *et al.* have reported the higher-order flower-shaped PAA formed by dropping the thermal-treated PAA solution into the

[a]*Department of Materials Science and Engineering, School of Materials and Chemical Technology, Institute of Science Tokyo, 2-12-1 S8-36 Ookayama Meguro-ku, Tokyo 152-8552, Japan. E-mail: nabae.y.aa@m.titech.ac.jp, hayakawa.t.ac@m.titech.ac.jp*

[b]*Materials Analysis Division, Core Facility Center, Research Infrastructure Management Center, Institute of Science Tokyo, 2-12-1 S7-26, Ookayama, Meguro-ku, Tokyo 152-8552, Japan*

† Electronic supplementary information (ESI) available. See DOI: https://doi.org/10.1039/d4lp00327f

poor solvent.[22,23] PIs have also been reported to form flower-like morphologies using the solvothermal method with commercially available monomers. This method involves heating the PAA precursor solution to a high temperature under high pressure after solution polymerization. Owing to their high carbon yield and well-preserved morphology after carbonization, PI FLPs have been used as precursors for carbon flowers.[7,24–30] However, the solvothermal method has only been successful in producing FLPs in the form of PIs.

In this study, we developed a novel synthetic route to PAA FLPs as the precursor of PI FLPs and carbon flowers. By constructing semiaromatic PAA, the difference in conformational entropy between the aromatic and alkyl segments can induce liquid-crystalline ordering, which opens up the potential for unique self-assembly behaviors.[31,32] Unlike in the solvothermal method, the flower-like morphology was achieved concurrently with the progression of precipitation polymerization at room temperature, initially forming PAA FLPs. Precipitation polymerization provides a straightforward bottom-up approach for producing uniform polymer particles. However, the precipitation polymerization of commercially available diamines and dianhydrides has previously only resulted in fine spherical PI microparticles.[33–35] Currently, there are no reports of PAA particles bearing complex three-dimensional, higher-order morphologies prepared through one-step precipitation polymerization. Notably, the particle size of the FLPs produced in this study could be tuned by adjusting the mixed solvent ratio. We attribute the formation of the flower-like morphology to the folding and stacking of the semiaromatic PAA synthesized in this study. The flower-like morphology remained well preserved after thermal imidization, with only particle size shrinkage observed following carbonization. The as-synthesized carbon flowers exhibited excellent catalytic activity for the 2-electron pathway oxygen reduction reaction (ORR), benefiting from their intricate hierarchical superstructure and nitrogen content.

Results and discussion

Precipitation polymerization of DA-6/PMDA

In this study, PAA particles were synthesized through precipitation polymerization involving bis(4-aminophenyl) 4,4′-(hexane-1,6-diylbis(oxy))dibenzoate (**DA-6**) and pyromellitic dianhydride (PMDA). **DA-6** was specifically designed with a flexible six-carbon alkyl segment at its center and rigid aromatic segments at both ends. **DA-6** was synthesized according to the procedure depicted in Scheme 1. First, **1** was synthesized *via* Williamson esterification of 1,6-dibromohexane and ethyl 4-hydroxybenzoate. This intermediate was then cleaved under basic conditions to yield the dicarboxylic acid of **2**, which was subsequently reacted with thionyl chloride to form the diacid chloride **3**. Next, **3** was esterified with 4-nitrophenol to produce dinitro **4**. Finally, **4** was hydrogenated to obtain diamine **DA-6**. PMDA, a commonly used dianhydride for PI synthesis, was selected to react with **DA-6** to introduce rigid segments into semiaromatic PAA (Scheme 2).

Precipitation polymerization requires the reaction solvent to be a good solvent for the monomers but a poor solvent for the resulting polymer. As the polymerization reaction progresses, polymeric microspheres form and precipitate out of the homogeneous solution. Acetone is commonly used as the solvent for the precipitation polymerization of PAA particles.[33,34] The **DA-6** synthesized in this study was insoluble in most common solvents, including ethanol (EtOH), ether, acetone, hexane, tetrahydrofuran (THF), chloroform, dichloromethane (DCM), toluene, ethyl acetate, chlorobenzene, acetonitrile, methyl ethyl ketone, and acetophenone (5 mg mL^{-1}). Meanwhile, it was soluble in 1-methyl-2-pyrrolidone (NMP), *N*,*N*-dimethylformamide (DMF), dimethyl sulfoxide (DMSO), *N*,*N*-dimethylacetamide (DMAc), and pyridine at room temperature (Table S1†). However, these solvents were not suitable for precipitation polymerization because they also dissolved the resulting PAA. **DA-6** is soluble in cyclohexanone and THF upon heating and remains dissolved upon cooling to room temperature. Therefore, precipitation polymerization was conducted using two different mixed solvent systems—cyclohexanone/toluene (cyc/tol) and cyclohexanone/acetone (cyc/ace)—and pure THF, with vigorous stirring at room temperature. In the mixed solvent systems, cyclohexanone served as the good solvent, while toluene and acetone acted as poor solvents. Precipitation polymerization began immediately after the monomer solutions were mixed. Previous studies have shown that solvents significantly influence the morphology of the resulting polymer particles.[16,18] Thus, we investigated the

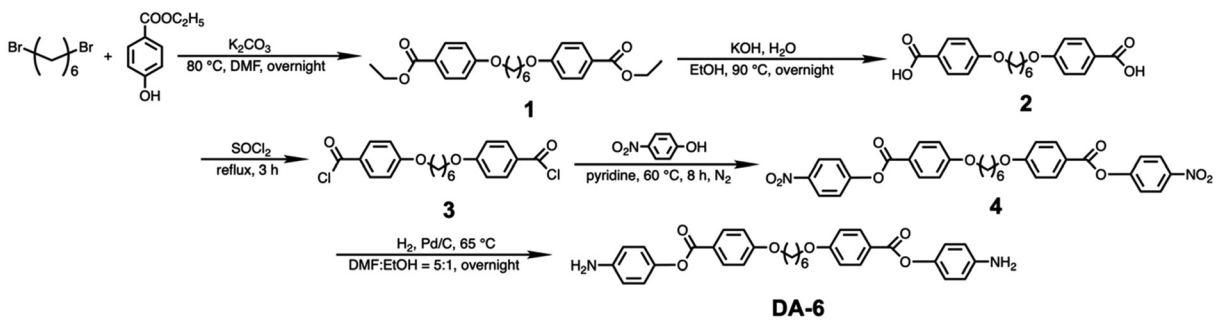

Scheme 1 Synthesis scheme of monomer **DA-6**.

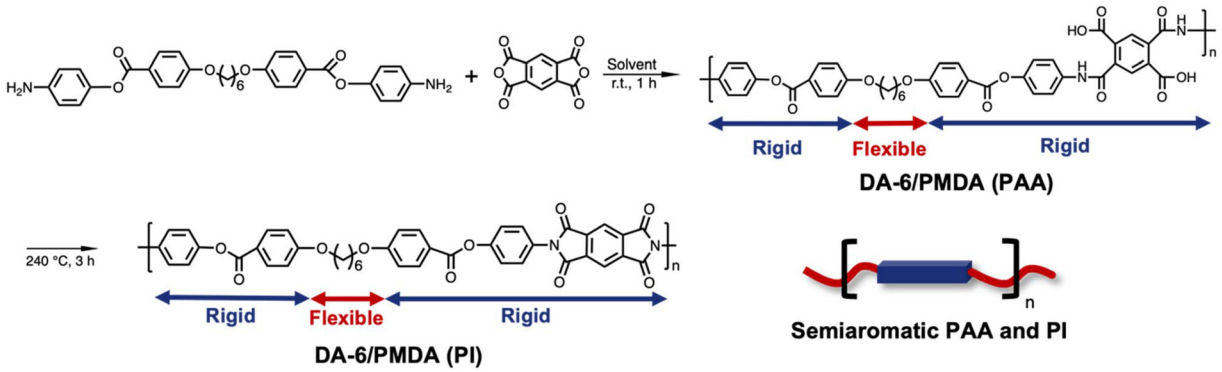

Scheme 2 Synthesis of PAA and corresponding PI from **DA-6** and PMDA. The illustrative image depicts the chemical structure of semiaromatic PAA and PI composed of flexible alkyl segments and rigid aromatic segments.

effect of the selected solvents on the particle morphology. For the mixed solvents, we varied the volume ratios, while maintaining a constant total solvent volume of 100 mL. The precipitation polymerization of **DA-6**/PMDA in pure THF resulted in coagulated and irregular multispheres (Fig. S1†).

When a cyc/tol mixed solvent was used, the resulting particles displayed a popcorn-like morphology with irregular sizes and shapes at cyc/tol ratios of 8 : 2, 7 : 3, and 3 : 7. In contrast, particles with minute flakes were observed at a cyc/tol ratio of 5 : 5. The effect of monomer concentration was further investigated at a cyc/tol ratio of 7 : 3. Increasing the monomer amount to 0.5 mmol and 1 mmol while maintaining the total solvent volume at 100 mL resulted in spherical particles with minute flaky surfaces, which could be considered as an incomplete flower-like morphology (Fig. S2†).

In contrast, when using cyc/ace as the mixed solvent, distinct FLPs consisting of interleaving nanoflakes were formed at cyc/ace ratios of 2 : 8, 3 : 7, 4 : 6, and 5 : 5 (Fig. 1a). However, when the acetone volume ratio was decreased to cyc/ace = 6 : 4, the flaky surface disappeared and the morphology transitioned to agglomerated spherical particles. With a further decrease in the acetone volume ratio to cyc/ace = 7 : 3, the independent particle morphology changed to irregular, hairy assemblies (Fig. S3†). The missing mixed volume ratios, such as 1 : 9 and 8 : 2, were not investigated because precipitation polymerization could not be established—either the monomer failed to dissolve or the polymer did not precipitate. Monomer concentration is another crucial factor that influences FLP morphology. When the **DA-6** monomer concentration was increased to 0.5 mmol while maintaining the total solvent volume at 100 mL with cyc/ace = 4 : 6 and 5 : 5, the flower-like morphology was observed again (Fig. S3†). The reaction time was maintained at 1 h to optimize yield, while the morphology became blurred when the reaction exceeded 1 h (Fig. S4†).

The inherent viscosity test indicated that PAA particles synthesized *via* precipitation polymerization in cyc/tol and cyc/ace exhibited relatively low molecular weights compared to PAA prepared through solution polymerization (Table S2†). In a precipitation polymerization, PAA exhibits low reactivity once solid particles precipitate under poor solvent conditions, thereby halting further polymerization and molecular weight growth. In contrast, solution polymerization occurs in a homogeneous system, allowing polymer molecules to interact continuously over an extended reaction time, resulting in a higher molecular weight.

The FLPs prepared in the cyc/ace solvent system exhibited a more developed flower-like morphology. Consequently, we selected these FLPs for subsequent thermal imidization and carbonization. Thermogravimetric analysis (TGA; Fig. S5†) of PAA FLPs revealed the two stages of weight loss corresponding to imidization and carbonization, respectively. The carbonization process began at approximately 336 °C, with a final yield of carbon flowers yield around 20%.

The FLPs demonstrated excellent thermal stability, and their morphology was well maintained after thermal imidization (Fig. 1b). Fourier transform infrared (FT-IR) spectra (Fig. S6a†) displayed absorption peaks corresponding to amide groups at 1661 cm^{-1} (C═O stretching) and 1543 cm^{-1} (C–N–H stretching) in the PAA FLPs, which disappeared after imidization. Additionally, absorption peaks corresponding to imide groups were observed at 1779 cm^{-1} (C═O stretching) and 1380 cm^{-1} (C–N–C stretching) in the PI FLPs, confirming that the imidization process was fully completed.

The PAA FLPs were subsequently carbonized under a N_2 atmosphere at a ramping rate of 1 °C min^{-1} to prevent morphological collapse (Fig. 1c). The cross-sectional images of the PI FLPs (Fig. 2a) and carbon flowers (Fig. 2b) prepared in the cyc/ace = 2 : 8 solvent system reveal an inner hollow morphology, confirming that the FLPs were formed from clusters of interleaving nanoflakes extending from the core to the surface. After carbonization, only size shrinkage was detected, which was attributed to the pyrolysis of the flexible alkyl segments.

Higher-order structure analysis of FLPs

The higher-order structure of the PAA FLPs was analyzed using wide-angle X-ray diffraction (WAXD), polarized optical microscopy (POM), and small-angle X-ray scattering (SAXS)

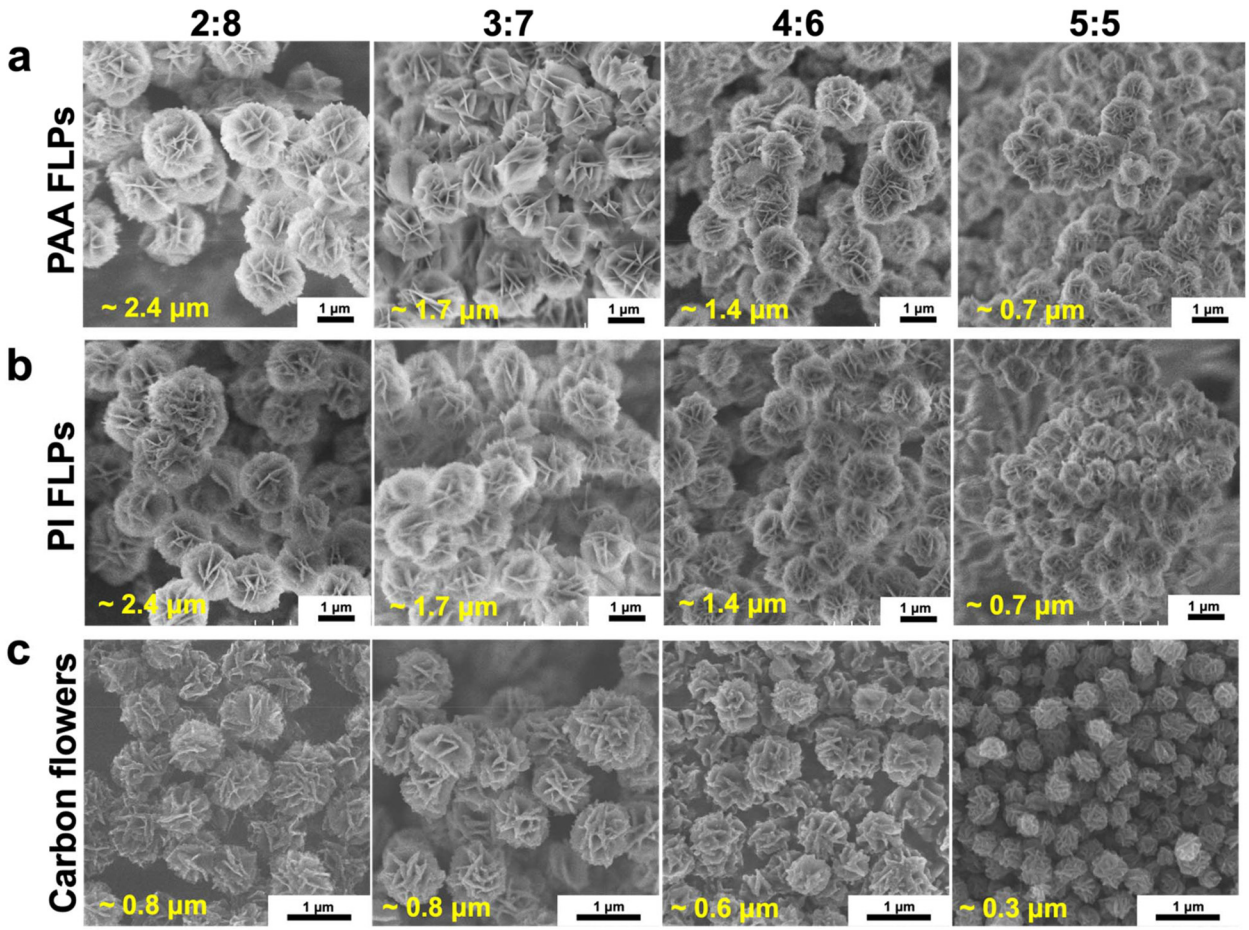

Fig. 1 Field emission scanning electron microscopy (FE-SEM) images of PAA FLPs (a), PI FLPs (b) and carbon flowers (c) prepared from **DA-6**/PMDA in cyc/ace with varied mixed solvent ratio.

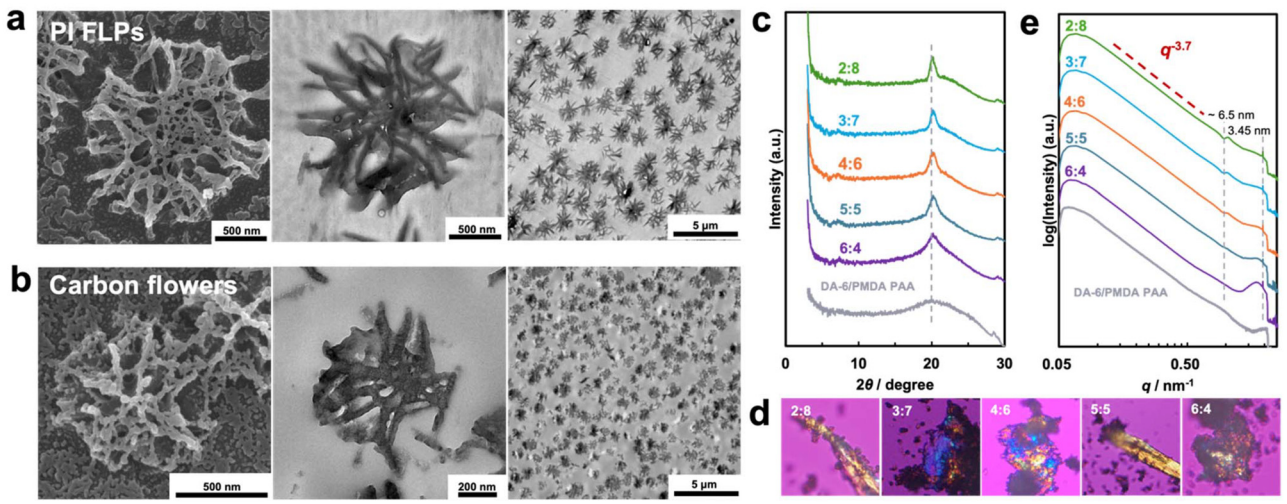

Fig. 2 Cross-section images of PI FLPs (a) and carbon flowers (b) prepared using in cyc/ace = 2 : 8 solvent system: FE-SEM images (left) and transmission electron microscopy (TEM) images (middle and right). (c) WAXD profiles of **DA-6**/PMDA particles prepared with different cyc/ace volume ratios compared to that of the **DA-6**/PMDA PAA prepared from solution polymerization. (d) POM images of FLPs prepared from cyc/ace solvent system observed at room temperature. (e) SAXS profiles of **DA-6**/PMDA particles prepared with different cyc/ace volume ratios compared to that of the **DA-6**/PMDA PAA prepared from homogenous solution polymerization.

with the **DA-6**/PMDA in the form of PAA and PI prepared from homogenous solution polymerization serving as a comparison.

The WAXD profile of the FLPs (Fig. 2c) presented sharp diffraction peaks at 2θ of approximately 20°, indicating the stacking of aromatic rings and an interchain distance of 0.44 nm for **DA-6**/PMDA molecules. The POM images of the FLPs prepared at room temperature using different cyc/ace volume ratios consistently exhibited anisotropic bright fields (Fig. 2d). Although differential scanning calorimetry (DSC) thermogram did not indicate any phase transition of PI FLPs between 30 and 300 °C (Fig. S7†), the results of WAXD and POM suggested the presence of a microcrystalline structure in the PAA FLPs.

SAXS profiles of FLPs prepared from cyc/ace solvent system are shown in Fig. 2e. A Bragg diffraction peak was observed at approximately 1.95 nm^{-1}. This result corresponds to a *d*-spacing of 3.22 nm, consistent with the repeating unit length indicated by the WAXD profile of the **DA-6**/PMDA PI bulk film at 2θ = 2.56° (Fig. S8a†). The SAXS profiles of the FLPs also exhibited a distinct oscillation signal at approximately 0.97 nm^{-1}, the oscillatory signal corresponds to a *d*-spacing of approximately 6.5 nm in the Porod region. This scattering region provides information about the primary structure corresponding to the shortest building block, namely, the minimal structural unit of lamellae forming the flower-like morphology. The petal thickness of the FLPs observed from FE-SEM was in the range of 20–40 nm, formed by the multiple stacking of these minimal structural units. In certain areas, a petal layer of approximately 6.5 nm was observed (Fig. S9†). The power-law region to the left of the Porod region exhibited a slope of −3.7, representing the surface fractal dimension of the particle surface.[19,34,36] Notably, the signal strength decreased as the flower-like morphology gradually became more blurred, eventually transitioning to completely spherical particles when prepared from cyc/ace = 6 : 4. The incomplete FLPs prepared with cyc/tol = 5 : 5 also exhibited a similar signal in this region (Fig. S10†). This unique oscillatory signal suggests the presence of a different higher-order structure than that of the **DA-6**/PMDA PAA or the PI bulk film prepared from solution polymerization.

Influence of solubility on FLP morphology

A gradual decrease in the particle size was observed in the PAA FLPs prepared from different cyc/ace volume ratios (Fig. 1a). Specifically, as the solubility of **DA-6**/PMDA decreased with increasing acetone volume ratio, precipitation formation occurred more rapidly, indicating increased crystalline rate. Under such conditions, the **DA-6**/PMDA molecules tended to attach randomly to the existing lamellae, forming branched lamellae under vigorous stirring. This resulted in larger particle sizes. The rapid formation of FLPs was confirmed within the first 15 minutes of the reaction (Fig. S4†). In contrast, the polymer chains diffused more effectively in a solvent with higher solubility, leading to relatively lower crystallization rate. Eventually, smaller FLPs with relatively compact layer-by-layer lamellae were formed (Fig. 3a). In comparison, the 4,4′-oxydianiline (ODA)/PMDA particles prepared under the same mixed solvent conditions exhibited smooth surfaces (Fig. S11†). The ODA/PMDA particle size was not influenced by the polymerization solvent, further suggesting that the size variation of the FLPs originated from the semiaromatic molecular structure and crystallization behavior of **DA-6**/PMDA in cyc/ace. The FLP petals varied slightly from loose to compact with increasing monomer concentration (Fig. S3†), which was also attributed to changes in the crystallization rate. Higher crystallization rate of **DA-6**/PMDA resulted in the formation of branched lamellae when the solubility of the system was reduced by increasing either the acetone volume ratio or monomer concentration. In contrast, higher solubility in the system promoted layer-by-layer growth, leading to densely packed FLPs (Fig. 3a).

Formation mechanism of DA-6/PMDA FLPs

The proposed self-assembly mechanism of PI FLPs prepared *via* the solvothermal method involves pressure- and temperature-induced crystallization of PI nanosheets.[7,12,25,27,28,30] Although an exclusive formation mechanism, synthetic route, solvent, or scaffold that specifically enables the fabrication of other polymeric FLPs is yet to be identified, some studies offer insights into how crystallization may contribute to the development of this fascinating flower-like morphology.[11–16,19]

Typically, the formation of polymer lamellae from solutions or melts is primarily governed by thermodynamic factors. The WAXD profile of **DA-6**/PMDA PAA prepared from homogenous solution exhibited an amorphous halo (Fig. 2c). In PI films prepared from drop-casting of PAA solution onto a substrate, the polymer chains tend to align in the in-plane parallel direction, which is influenced by shrinkage due to the clamping effect at the film edges during thermal imidization[37] and the repeating unit length and interchain distance of the **DA-6**/PMDA bulk film were investigated using the WAXD profiles (Fig. S8a† and Fig. 3b). In contrast to the bulk films, **DA-6**/PMDA FLPs exhibited a distinct crystalline behavior, with the petals intersecting to form a fractal morphology. This unique microcrystalline flower-like structure was formed *via* precipitation polymerization in a poor solvent at room temperature, suggesting that the crystalline process of FLPs in this study was more kinetically driven rather than thermodynamically controlled.

In summary, (1) the WAXD profile and POM images confirm the presence of a microcrystalline structure in the FLPs (Fig. 2c and d). (2) The FLP SAXS profiles display unique oscillatory valleys at approximately 0.97 nm^{-1} (Fig. 2e), indicating a different chain arrangement compared to the structures of bulk PI films and spherical particles. The corresponding *d*-spacing of approximately 6.5 nm, which is related to the building block thickness of the flower-like morphology, is approximately twice the length of the repeating unit. (3) Comparative precipitation polymerization of ODA/PMDA in a cyc/ace system yielded only fine spherical particles under conditions that produced FLPs with **DA-6**/PMDA. This suggests that the unique molecular design of semiaromatic **DA-6**/PMDA

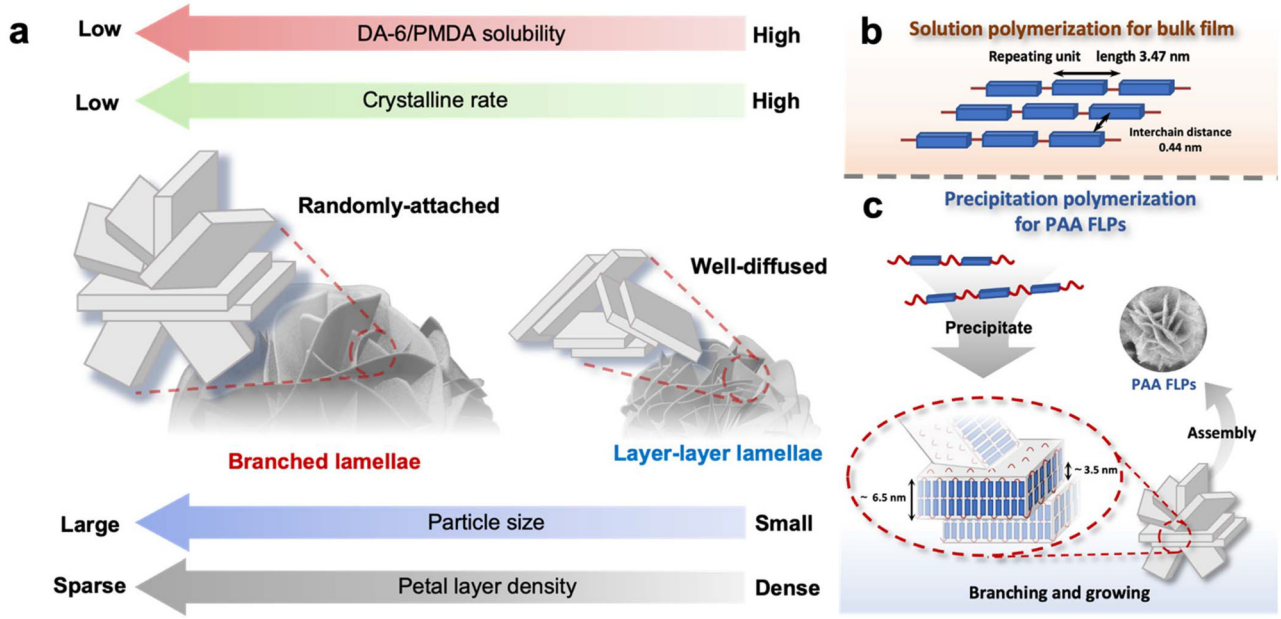

Fig. 3 (a) Influence of system solubility on FLP morphology. (b) Comparison of the chain alignments of the bulk film and FLPs: parallel molecular chain alignment in the PI bulk film and (c) folding and stacking chain alignment in the PAA FLPs, illustrating the proposed formation mechanism of this study, suggesting that the size variation of the FLPs originated from the semiaromatic molecular structure and crystallization behavior of **DA-6**/PMDA in cyc/ace.

leads to the formation of a flower-like morphology. Based on these observations, we propose that the formation mechanism of the FLPs in this study (Fig. 3c) follows a branching mechanism similar to those of PAN and PI FLPs prepared *via* solvothermal methods.[38] The flexible alkyl segments in **DA-6**/PMDA allow the PAA chains to fold and stack to form lamellar petals. These lamellae grow on existing petals or branches to create an intersecting, fractal morphology that ultimately assembles into FLPs.

ORR performance of carbon flowers

H_2O_2 is one of the most important industrial chemicals due to its broad range of applications, including paper and textile manufacturing, wastewater treatment, and more.[39,40] Currently, its industrial production primarily relies on the anthraquinone oxidation process, which involves energy-intensive multistep reactions and generates hazardous by-products.[41] As an alternative, electrochemical H_2O_2 production *via* the 2-electron ORR at a lower potential (0.7 V *vs.* RHE) can offer a more sustainable and environmentally friendly approach.[42]

Oxygen molecules can also be reduced to H_2O *via* the 4-electron pathway, a process that releases a relatively large free energy (1.23 V *vs.* RHE) and is widely utilized in fuel cells. However, a 2 + 2 reduction pathway has been identified, originating from the 2-electron ORR.[43,44] Therefore, understanding the 2-electron ORR is not only essential for sustainable H_2O_2 production but also provides deeper insights into the 2 + 2 reduction pathway, which is relevant for practical fuel cell applications.

So far, efforts have been made to improve the catalytic activity and control the catalytic selectivity, such as using the metal-free mesoporous N-doped carbon.[45,46] Carbon flowers made from PAN have also been reported to have high selectivity and activity in the production of H_2O_2 in a KOH electrolyte through the 2-electron ORR.[47]

To evaluate the 2-electron ORR activity of carbon flowers prepared in this work, rotating ring disk electrode (RRDE) voltammetry was conducted in O_2-saturated 0.5 M H_2SO_4 at a rotation rate of 1600 rpm. Carbon flowers synthesized from cyc/ace = 2 : 8 with a particle size around 0.8 μm were selected as the representative sample. For comparison, amorphous carbon with the same chemical composition as carbon flowers (Fig. 4a)—carbonized from PAA particles prepared in cyc/tol = 7 : 3 (Fig. S2†)—as well as commercially available Ketjen Black (KB), were also included.

The RRDE voltammogram is shown in Fig. 4b–d. Among all candidates, carbon flowers exhibited the highest 2-electron reduction activity. They also demonstrated the highest half-wave potential of 0.25 V *vs.* RHE, compared to 0.20 V for amorphous carbon and 0.08 V for KB (Fig. 4c and Table S3†). The superior 2-electron reduction activity of carbon flowers was attributed to their nitrogen content (C: 93.24%, N: 2.72%, H: 0.78%, determined by elemental analysis). Additionally, their unique open flower-like morphology facilitated efficient mass transport of the generated H_2O_2 and suppressed another 2-electron reduction from H_2O_2 to H_2O,[45] contributing to their high H_2O_2 selectivity of nearly 80% at a wide range of potentials (Fig. 4b and d).

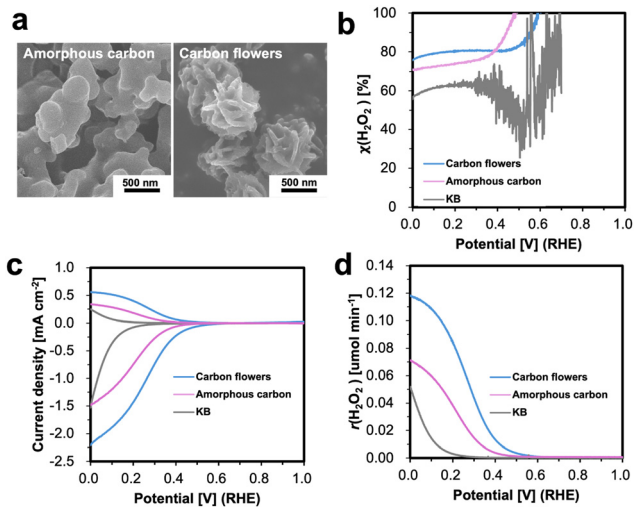

Fig. 4 (a) FE-SEM images of amorphous carbon and carbon flowers. The amorphous carbon was carbonized from popcorn-like PAA particles with irregular sizes and shapes prepared in cyc/tol = 7 : 3. The particle morphology became further coagulated under the same carbonization condition where PAA FLPs maintained the flower-like morphology. (b) H_2O_2 selectivity of carbon flower, amorphous carbon, and KB. (c) RRDE voltammograms of carbon flower, amorphous carbon, and KB in O_2-saturated 0.5 M H_2SO_4 electrolyte with a catalyst load of 60 μg cm^{-2}. (d) H_2O_2 production rate of carbon flower, amorphous carbon and KB.

Conclusions

In this study, **DA-6**/PMDA PAA FLPs were synthesized as precursors through a one-step precipitation polymerization in a cyc/ace mixed solvent. Unlike the conventional solvothermal method, the as-synthesized PAA FLPs were formed directly during polymerization at room temperature. The development of the flower-like morphology was attributed to rapid crystalline formation under poor solubility conditions. The branched growth of the **DA-6**/PMDA microcrystals into fractal petals was enhanced in solvents with lower solubility, resulting in larger FLPs with a more distinct fractal morphology. The flower-like structure was well preserved after thermal imidization and carbonization, although particle size shrinkage was observed in the carbon flowers. We propose that the flower-like structure arises from folding and stacking of the molecular alignments of **DA-6**/PMDA. This work offers a facile method of producing carbon flowers from PAA FLPs, which also deepens the understanding of the self-assembly behavior of PAA prepared from polycondensation. The as-synthesized carbon flowers exhibited excellent electrocatalytic activities and selectivity for H_2O_2 production *via* 2-electron pathway, attributed to its nitrogen content and unique flower-like morphology. Carbon flowers with hierarchical superstructures are expected to exhibit high activity in various fields, including energy conversion and storage devices, such as electrocatalyst supports, supercapacitors, and gas storage materials.

Experimental

Materials

Ethyl 4-hydroxyl benzoate, 1,6-dibromohexane, and 4,4′-oxydianiline (ODA) were purchased from Tokyo Chemical Industry (TCI, Japan). The ODA was recrystallized from EtOH prior to use. PMDA was purchased from Nippon Shokubai and recrystallized from acetic anhydride before use. Cyclohexanone, acetone, toluene, NMP, and THF (stabilizer-free) were purchased from Fujifilm Wako Pure Chemical Industries. All other chemicals were of reagent grade and used as received.

Synthesis of DA-6

Dimethyl 4,4′-(dodecane-1,12-diylbis(oxy))dibenzoate (1). Ethyl 4-hydroxyl benzoate (36.52 g, 240 mmol) was dissolved in DMF (250 mL) in the presence of K_2CO_3 (41.46, 300 mmol), and stirred at room temperature for 30 min. Next, 1,6-dibromohexane (15.56 mL, 100 mmol) was added dropwise, and the reaction mixture was stirred at 80 °C under reflux overnight. The reaction mixture was cooled and precipitated with deionized H_2O followed by EtOH. After filtration by suction, the resulting white powder was dried under vacuum at 70 °C (yield: 95%). Proton nuclear magnetic resonance (^{1}H NMR) (400 MHz, $CDCl_3$, δ, ppm): 8.01–7.92 (m, 2H, Ar*H*), 6.93–6.85 (m, 2H, Ar*H*), 4.01 (t, J = 6.4 Hz, 2H, –CH_3), 3.87 (s, 3H, –O–CH_2–), 1.89–1.77 (m, 2H, –CH_2–), 1.54 (dq, J = 7.4, 3.5 Hz, 2H, –CH_2–). FT-IR (KBr, ν, cm^{-1}), 3050, 2980, 2942, 2908, 2871, 1710, 1605, 1510, 1473, 1444, 1419, 1395, 1366, 1315, 1277, 1248, 1171, 1132, 1108, 1026, 856, 811, 772, 735, 698, 644, 632, 516, 496, 465, 445, 410 cm^{-1}.

4,4′-(Dodecane-1,12-diylbis(oxy))dibenzoic acid (2). **1** (20.72 g, 50 mmol) and KOH (13.47 g, 240 mmol) were added to a mixed solvent of EtOH/H_2O (250 mL/40 mL). The reaction mixture was stirred at 90 °C under reflux overnight and then cooled to room temperature. Subsequently, 25 mL HCl (36%, w/w, aq.) was added, and the mixture was stirred for 4 h. The product was isolated *via* filtration and washed with EtOH. The resulting white powder was dried under vacuum at 80 °C. The product was further purified through recrystallization in a DMF/EtOH mixed solvent (yield: 94%). ^{1}H NMR (400 MHz, DMSO-D_6, δ, ppm), 12.64 (s, 1H, –COO*H*), 7.92–7.83 (m, 1H, Ar*H*), 7.04–6.96 (m, 1H, Ar*H*), 4.05 (t, J = 6.5 Hz, 1H, –O–CH_2–), 1.76 (p, J = 6.6 Hz, 1H, –CH_2–), 1.52–1.44 (m, 1H, –CH_2–). FT-IR (KBr, ν, cm^{-1}) : 2941, 2861, 2666, 2560, 1809, 1681, 1606, 1577, 1513, 1469, 1429, 1389, 1330, 1295, 1254, 1169, 1119, 1072, 1050, 1024, 993, 942, 885, 847, 770, 693, 647, 552, 506 cm^{-1}.

4,4′-(Dodecane-1,12-diylbis(oxy))dibenzoyl chloride (3):. **2** (25.78 g, 70 mmol) was dissolved in $SOCl_2$ (110 mL), and the solution was heated to 90 °C under reflux for 3 h. After cooling to room temperature, excess $SOCl_2$ was removed *via* vacuum distillation. The remaining powder was washed with hexane and filtered by suction. The resulting white powder was dried under vacuum at 60 °C (yield: 99%). ^{1}H NMR (400 MHz, $CDCl_3$, δ, ppm), 8.12–8.03 (m, 1H, Ar*H*), 6.99–6.91 (m, 1H, Ar*H*), 4.07 (t, J = 6.3 Hz, 1H, –O–CH_2–), 1.87 (pd, J = 6.5, 3.7 Hz, 1H, –CH_2–), 1.64–1.51 (m, 1H, –CH_2–). FT-IR (KBr, ν,

cm^{-1}): 3412, 3100, 2944, 2871, 1769, 1740, 1674, 1599, 1508, 1473, 1426, 1395, 1314, 1265, 1213, 1167, 1124, 1013, 872, 847, 808, 775, 731, 646, 623, 541, 502 cm^{-1}.

Bis(4-nitrophenyl) 4,4′-(dodecane-1,12-diylbis(oxy))dibenzoate (4). First, 4-nitrophenol (8.90 g, 64 mmol) was dissolved in pyridine (24 mL) in a well-dried two-necked flask and stirred under a N_2 atmosphere in an ice bath for 1 h. The pyridine solution (24 mL) of **3** (6.32 g, 16 mmol) was stabilized at room temperature and added dropwise to the nitrophenol/pyridine solvent. The reaction mixture was stirred at 60 °C under reflux overnight. After completion, the target product was collected by reprecipitation in EtOH. The resultant white precipitate was collected *via* filtration and dried under vacuum at 80 °C. The product was further purified by silica column chromatography using DCM and subsequently washed with EtOH (yield: 70%). ^{1}H NMR (400 MHz, $CDCl_3$, δ, ppm), 8.36–8.28 (m, 1H, Ar*H*), 8.19–8.10 (m, 1H, Ar*H*), 7.45–7.36 (m, 1H, Ar*H*), 7.04–6.96 (m, 1H, Ar*H*), 4.09 (t, J = 6.4 Hz, 1H, –O–CH_2–), 1.89 (q, J = 6.6 Hz, 1H, –CH_2–), 1.64–1.56 (m, 1H, –CH_2–). FT-IR (KBr, ν, cm^{-1}): 3080, 2947, 2359, 1743, 1732, 1604, 1588, 1523, 1488, 1347, 1312, 1253, 1213, 1169, 1110, 1067, 1051, 1006, 862, 844, 759, 688, 673 cm^{-1}.

Bis(4-aminophenyl) 4,4′-(dodecane-1,12-diylbis(oxy))dibenzoate (DA-6). **4** (7.22 g, 12 mmol) was dissolved in DMF/EtOH (168 mL, 5/1, v/v) in the presence of Pd/C (0.24 g) as the catalyst. The reaction mixture was refluxed under a hydrogen atmosphere at 65 °C overnight. After completion, the catalyst residue was removed by hot filtration through Celite. The filtrate was re-precipitated in EtOH, collected by filtration, and dried under vacuum at 100 °C for 12 h. The product was further purified by recrystallization from dichloroethane (yield: 87%). The total yield of **DA-6** synthesized over the five steps was 49%. ^{1}H NMR (400 MHz, DMSO-D_6, δ, ppm), 8.06–7.98 (m, 1H, Ar*H*), 7.13–7.05 (m, 1H, Ar*H*), 6.90–6.82 (m, 1H, Ar*H*), 6.62–6.54 (m, 1H, Ar*H*), 5.08 (s, 1H, –NH_2), 4.09 (t, J = 6.4 Hz, 1H, –O–CH_2–), 1.79 (t, J = 6.5 Hz, 1H, –CH_2–), 1.55–1.46 (m, 1H, –CH_2–). FT-IR (KBr, ν, cm^{-1}): 3612, 3443, 3365, 3080, 2945, 2875, 2855, 1924, 1703, 1605, 1511, 1470, 1422, 1396, 1315, 1257, 1188, 1169, 1123, 1083, 1023, 1010, 992, 922, 874, 849, 827, 798, 768, 696, 648, 535, 519 cm^{-1}.

Precipitation polymerization of DA-6/PMDA

DA-6 is soluble in cyclohexanone and THF upon heating and remains dissolved upon cooling to room temperature. Therefore, THF and cyclohexanone were selected as the candidate solvents for the precipitation polymerization of **DA-6** and PMDA. However, the resulting PAA did not precipitate in pure cyclohexanone. Therefore, to identify a suitable solvent, precipitation polymerization was conducted using three solvent systems: pure THF, cyc/tol, and cyc/ace.

Precipitation polymerization of DA-6/PMDA in THF

First, 50 mL THF was added to **DA-6** (0.25 mmol, 0.1352 g) in a 100 mL round-bottom flask and heated at 70 °C until complete dissolution. The **DA-6**/THF solution was then cooled to room temperature in the air. Separately, an equimolar ratio of PMDA (0.25 mmol, 0.0545 g) was dissolved in 50 mL THF in a 500 mL round-bottom flask and stirred for 30 min. Once the monomer was well dissolved and dispersed, the **DA-6**/THF solution was added to the PMDA solution, and the mixture was vigorously stirred at room temperature for 1 h under a N_2 atmosphere. The PAA particles were collected using a rotary evaporator and subsequently dried under vacuum at 40 °C overnight to obtain pale yellow PAA particles.

Precipitation polymerization in cyc/tol mixed solvent

First, 50 mL cyc/tol mixed solvent (volume ratio, 8 : 2, 7 : 3, 5 : 5, 3 : 7) was added to **DA-6** (0.25 mmol, 0.1352 g; 0.5 mmol, 0.2704 g; 1 mmol 0.5408 g) in a 100 mL round-bottom flask and heated until complete dissolution. The **DA-6** solution was then cooled to room temperature in air. Separately, an equimolar ratio of PMDA (0.25 mmol, 0.0545 g; 0.5 mmol 0.1090 g; 1 mmol 0.2182 g) was dissolved in 50 mL of the same cyc/tol mixed solvent in a 500 mL round-bottom flask and stirred for 30 min at room temperature. Once the monomer was well dissolved and dispersed, the **DA-6** solution was added to the PMDA solution. The mixture was then vigorously stirred at room temperature for 1 h under a N_2 atmosphere. The PAA particles were collected by centrifugal separation and washed thrice with toluene. After removing the toluene with a rotary evaporator, the powder was dried under vacuum at 40 °C overnight to obtain the pale yellow PAA particles.

Precipitation polymerization in cyc/ace mixed solvent

DA-6 (0.25 mmol, 0.1352 g) was dissolved in 20 mL cyclohexanone in a 100 mL round-bottom flask and heated until complete dissolution. The **DA-6**/cyclohexanone solution was then cooled to room temperature in air. Separately, an equimolar ratio of PMDA (0.25 mmol, 0.0545 g) was dissolved in 80 mL acetone in a 500 mL round-bottom flask. Once the monomer was completely dissolved and dispersed, the **DA-6** solution was added to the PMDA solution, and the mixture was vigorously stirred at room temperature for 1 h under a N_2 atmosphere. PAA particles were collected by centrifugal separation and washed thrice with acetone. After removing the acetone using a rotary evaporator, the powder was dried at 40 °C under vacuum overnight to obtain PAA particles. The same procedure was employed to conduct the precipitation polymerization of **DA-6**/PMDA using different cyc/ace volume ratios (3 : 7, 4 : 6, 5 : 5, 6 : 4, and 7 : 3) and with a different **DA-6** concentration (0.5 mmol).

FT-IR (KBr, ν, cm^{-1}): 3450, 3073, 2937, 2865, 1726, 1661, 1607, 1543, 1510, 1412, 1259, 1209, 1199, 1167, 1113, 1074, 1013, 877, 845, 805, 763, 694, 652, 605, 523 cm^{-1}, as shown in Fig. S5a.† ^{1}H NMR (400 MHz, DMSO-D_6) spectra is shown in Fig. S5b.†

Precipitation polymerization of ODA/PMDA (0.25 mmol) was conducted similarly in the cyc/ace mixed solvent.

Imidization and carbonization

The pale brown powder of PI particles was obtained by heating the **DA-6**/PMDA PAA particles at 240 °C for 3 h under vacuum.

IR (KBr, ν, cm^{-1}): 3444, 2933, 2862, 1779, 1727, 1606, 1512, 1468, 1380, 1259, 1210, 1166, 1122, 1073, 1013, 874, 845, 801, 760, 723, 692, 643, 523 cm^{-1}.

To convert the PAA particles into carbon particles, the PI particles were carbonized under N_2 (50 mL min^{-1}) at a ramping rate of 1 °C min^{-1} and held at 900 °C for 30 min.

Preparation of DA-6/PMDA bulk film

DA-6/PMDA bulk film were synthesized through a two-step step-growth polymerization between **DA-6** and PMDA. **DA-6** (497 mg) was added to a 25 mL two-necked flask and dissolved by 1.5 mL NMP under N_2 atmosphere. PMDA (200.45 mg) was then added to the flask. After adding another 1.5 mL NMP, the reaction solvent was stirred under Argon atmosphere at room temperature for 24 h. The PI film of **DA-6**/PMDA was obtained by casting the reaction solvent onto a flat glass schale, ventilated and heated on a hot plate at 80 °C for 1 h before completely imidized at 240 °C for 3 h under vacuum.

Characterization

^1H NMR spectra were obtained using a JEOL 400 MHz NMR instrument. FT-IR spectra were recorded on a JASCO FT-IR 4100 spectrometer using the KBr pellet method. The inherent viscosities (η_{inh}) of PAAs with a solid content of 0.5 g dL^{-1} were measured in *N*-methyl-2-pyrrolidone (NMP) at 30 °C using an Ostwald viscometer. FE-SEM was conducted using an S-5500 microscope (Hitachi High-Tech Corporation) at an accelerating voltage of 1.0–3.0 kV and the cross-section images were gained from S4700 (Hitachi High-Tech Corporation) operated at 6.0 kV. To obtain cross-sections, samples were embedded in light curable resin (Toagosei LCR-D800) and sectioned using an ultramicrotome. Subsequently, the block faces were plasma etched using a PIB-20 (Vacuum Device) to remove the resin. TEM images were obtained on a H7650 Zero. A (Hitachi High-Tech Corporation) at a 100 kV accelerating voltage. For TEM analysis, samples were embedded in epoxy resin, and then sectioned using an ultramicrotome (Leica Microsystems EM UC7). TGA was performed using an EXSTAR TG/DTA 7300 (Seiko Instruments, Tokyo, Japan) at a heating rate of 1 °C min^{-1}. The optical structure of PAA was observed using a POM (OLYMPUS BX51). SAXS was conducted at the SPring-8 beamline BL40B2 with a wavelength of 1.9 Å and a Pilatus detector. WAXD was performed using a Bruker New D8 DISCOVER instrument. X-rays generated by a Bruker AXS NanoSTAR (output: 50 kV, 100 mA) were converted to monochromatic X-rays using a Göbel mirror, and the sample was irradiated with focused CuKα rays (wavelength: 1.5416 Å). The C, H, and N contents of the carbon flower were determined using a CHN elemental analyzer (J-Science Lab, JM10).

Electrochemical study

The catalytic activity of the samples was evaluated using cyclic voltammetry (CV, 10 mV s^{-1}) with a RRDE, sweeping the disk potential between 0 V to 1.0 V *vs.* RHE. The 3 mg of catalyst powder was ultrasonically dispersed in a mixture of Nafion solution (5 wt%, DEC520, FUJIFILM, 45 μL), ethanol (300 μL), ultrapure water (300 μL) and then was applied to the surface of a glassy carbon electrode. The amount of catalyst loading was 60 μg cm^{-2}. The rotation speed of the RRDE was controlled with an RRDE system (NIKKO KEISOKU, RDE-1) and the electrochemical data were collected with a potentiostat (HZ-700, HAG1232m). CV was first performed in N_2-saturated H_2SO_4 (0.5 M) for cleaning and background, and then in O_2-saturated H_2SO_4. The ORR current was determined by subtracting the N_2 current from the O_2 current. The potential of the Pt ring electrode was kept at 1.2 V *vs.* RHE for the detection of H_2O_2 produced on the disk electrode and the selectivity for the two-electron reduction, $\chi(H_2O_2)$, was calculated using the following equation:

$$\chi(H_2O_2)(\%) = 2 \times \frac{\frac{I_R}{N}}{I_D + \frac{I_R}{N}} \times 100.$$

The electron transfer number was determined by the ratio of current density for the ring/disk electrode using the following equation:

$$n = \frac{4 \times I_D}{I_D + \frac{I_R}{N}}$$

where the I_D is the disk current, I_R is the ring current, and N the collection factor, which was theoretically and experimentally pre-determined as 0.37.

Author contributions

Y. C. contributed to the investigation, data visualization, and writing the original draft. R. K. was involved in the investigation. K. H. participated in reviewing and editing the manuscript. Y. N. was responsible for conceptualization, funding acquisition, and manuscript review and editing. T. H. contributed to the conceptualization, supervision, and review and editing of the manuscript.

Data availability

The data supporting this article have been included as part of the article and its ESI.†

Conflicts of interest

There are no conflicts to declare.

Acknowledgements

This study was financially supported by JSPS KAKENHI (21K04828) and the New Energy and Industrial Technology Development Organization (NEDO).

FE-SEM was performed using equipment shared through the MEXT Project (JPMXS0420900521). CHN elemental analysis was performed under the assistance of Materials Analysis Division, Core Facility Center, Research Infrastructure Management Center. SAXS measurements were carried out at BL40BII at SPring-8 (Proposal Number 2023A1197, 2024B1228) with the assistance of Prof. Tomoyasu Hirai (Osaka Institute of Technology) and Dr Noboru Ohota (JASRI). Y. Chen is supported by a Tokyo Tech Tsubame Scholarship and Scholarships from the Amano Institute of Technology.

References

1 J. X. Liu, N. Bizmark, D. M. Scott, R. A. Register, M. P. Haataja, S. S. Datta, C. B. Arnold and R. D. Priestley, *JACS Au*, 2021, **1**, 936–944.
2 C. Li, H. Peng, J. Cai, L. Li, J. Zhang and Y. Mai, *Adv. Mater.*, 2021, **33**, 1–10.
3 J. Lee, K. H. Ku, J. Kim, Y. J. Lee, S. G. Jang and B. J. Kim, *J. Am. Chem. Soc.*, 2019, **141**, 15348–15355.
4 D. Klinger, C. X. Wang, L. A. Connal, D. J. Audus, S. G. Jang, S. Kraemer, K. L. Killops, G. H. Fredrickson, E. J. Kramer and C. J. Hawker, *Angew. Chem., Int. Ed.*, 2014, **53**, 7018–7022.
5 D. Varadharajan, H. Turgut, J. Lahann, H. Yabu and G. Delaittre, *Adv. Funct. Mater.*, 2018, **28**, 1800846.
6 L. Tong, Y. Nabae, T. Hirai, H. Yabu and T. Hayakawa, *Macromol. Chem. Phys.*, 2023, **224**, 2200402.
7 M. Sharma and M. A. Snyder, *Microporous Mesoporous Mater.*, 2022, **335**, 111801.
8 H. Sun, Z. Chu, D. Hong, G. Zhang, Y. Xie, L. Li and K. Shi, *J. Alloys Compd.*, 2016, **658**, 561–568.
9 Z. Wang, H. Yu, K. Ma, Y. Chen, X. Zhang, T. Wang, S. Li, X. Zhu and X. Wang, *Bioconjugate Chem.*, 2018, **29**, 2090–2099.
10 J. Li, M. Zhang, Z. Song, S. Liu, J. Wang and L. Zhang, *Catalysts*, 2019, **9**, 767.
11 T. Nakanishi, K. Ariga, T. Michinobu, K. Yoshida, H. Takahashi, T. Teranishi, H. Möhwald and D. G. Kurth, *Small*, 2007, **3**, 2019–2023.
12 J. Yin, J. Yan, M. He, Y. Song, X. Xu, K. Wu and J. Pei, *Chem. – Eur. J.*, 2010, **16**, 7309–7318.
13 H. Zhao, X. Guo, S. He, X. Zeng, X. Zhou, C. Zhang, J. Hu, X. Wu, Z. Xing, L. Chu, Y. He and Q. Chen, *Nat. Commun.*, 2014, **5**, 3108.
14 H. Zhu, T. J. Buchtal and M. Mitsuishi, *Appl. Surf. Sci.*, 2021, **563**, 150245.
15 X. Liu, M. A. Moradi, T. Bus, M. G. Debije, S. A. F. Bon, J. P. A. Heuts and A. P. H. J. Schenning, *Angew. Chem., Int. Ed.*, 2021, **60**, 27026–27030.
16 K. Zhang, A. Geissler, X. Chen, S. Rosenfeldt, Y. Yang, S. Förster and F. Müller-Plathe, *ACS Macro Lett.*, 2015, **4**, 214–219.
17 Z. Chen, J. Huang, Y. Cui and R. Fu, *Carbon*, 2022, **190**, 395–401.
18 S. Chen, D. M. Koshy, Y. Tsao, R. Pfattner, X. Yan, D. Feng and Z. Bao, *J. Am. Chem. Soc.*, 2018, **140**, 10297–10304.
19 H. Gong, J. Ilavsky, I. Kuzmenko, S. Chen, H. Yan, C. B. Cooper, G. Chen, Y. Chen, J. A. Chiong, Y. Jiang, J. Lai, Y. Zheng, K. H. Stone, L. Huelsenbeck, G. Giri, J. B. H. Tok and Z. Bao, *J. Am. Chem. Soc.*, 2022, **144**, 17576–17587.
20 C. B. Arrington, D. A. Rau, J. A. Vandenbrande, M. Hegde, C. B. Williams and T. E. Long, *ACS Macro Lett.*, 2021, **10**, 412–418.
21 M. Lahnsteiner, M. Caldera, H. M. Moura, D. A. Cerrón-Infantes, J. Roeser, T. Konegger, A. Thomas, J. Menche and M. M. Unterlass, *J. Mater. Chem. A*, 2021, **9**, 19754–19769.
22 H. Sun and J. Du, *Macromolecules*, 2020, **53**, 11033–11039.
23 H. Sun, X. Li, K. Jin, X. Lai and J. Du, *Nanoscale Adv.*, 2022, **4**, 1422–1430.
24 H. Peng, S. Qi, Q. Miao, R. Zhao, Y. Xu, G. Ma and Z. Lei, *J. Power Sources*, 2021, **482**, 228993.
25 Y. Wang, Y. Lu, X. Liu, H. Chi, J. Hu, H. Zhao and G. Xiao, *J. Energy Storage*, 2022, **47**, 103656.
26 G. Zhao, G. Zou, X. Qiu, S. Li, T. Guo, H. Hou and X. Ji, *Electrochim. Acta*, 2017, **240**, 24–30.
27 M. J. Taublaender, M. Reiter and M. M. Unterlass, *Macromolecules*, 2019, **52**, 6318–6329.
28 Z. Xu, X. Zhuang, C. Yang, J. Cao, Z. Yao, Y. Tang, J. Jiang, D. Wu and X. Feng, *Adv. Mater.*, 2016, **28**, 1981–1987.
29 M. Wang, W. J. Bao, J. Wang, K. Wang, J. J. Xu, H. Y. Chen and X. H. Xia, *Sci. Rep.*, 2014, **4**, 6606.
30 J. Liu, T. Wang and H. Sun, *ACS Macro Lett.*, 2024, **13**, 1139–1146.
31 J. K. Kallitsis and A. K. Andreopoulou, in *Polymer Science: A Comprehensive Reference*, ed. K. Matyjaszewski and M. Möller, Elsevier, Amsterdam, 2012, pp. 725–773..
32 B. D. Olsen and R. A. Segalman, *Mater. Sci. Eng., R*, 2008, **62**, 37–66.
33 K. Asao, *J. Photopolym. Sci. Technol.*, 2014, **27**, 181–185.
34 S. Kuretani, Y. Nabae and T. Hayakawa, *J. Photopolym. Sci. Technol.*, 2022, **35**, 271–276.
35 K. Hatakeyama-Sato, H. Ishikawa, S. Takaishi, Y. Igarashi, Y. Nabae and T. Hayakawa, *Polym. J.*, 2024, **56**, 977–986.
36 H. Matsuoka, *J. Jpn. Oil Chem. Soc.*, 2000, **49**, 1163–1171.
37 Y. Nagata, Y. Ohnishi and T. Kajiyama, *Polym. J.*, 1996, **28**, 980–985.
38 H. Gong, S. Chen, J. B. H. Tok and Z. Bao, *Matter*, 2023, **6**, 2206–2234.
39 A. Yu, S. Liu and Y. Yang, *Chem. Commun.*, 2024, **60**, 5232–5244.
40 S. Li, J. Ma, F. Xu, L. Wei and D. He, *Chem. Eng. J.*, 2023, **452**, 139371.
41 J. M. Campos-Martin, G. Blanco-Brieva and J. L. G. Fierro, *Angew. Chem., Int. Ed.*, 2006, **45**, 6962–6984.
42 K. Otsuka and I. Yamanaka, *Electrochim. Acta*, 1990, **35**, 319–322.
43 T. S. Olson, S. Pylypenko, J. E. Fulghum and P. Atanassov, *J. Electrochem. Soc.*, 2010, **157**, B54–B63.

44 Y. Wu and Y. Nabae, *Curr. Opin. Electrochem.*, 2021, **25**, 100633.
45 J. Park, Y. Nabae, T. Hayakawa and M. A. Kakimoto, *ACS Catal.*, 2014, **4**, 3749–3754.
46 Y. Wu, A. Muthukrishnan, S. Nagata and Y. Nabae, *J. Phys. Chem. C*, 2019, **123**, 4590–4596.
47 H. Gong, L. Wei, S. Chen, Z. Chen, T. F. Jaramillo and Z. Bao, *Nano Res.*, 2023, **16**, 11556–11563.